

EXTRACTING BIAS USING THE CROSS-BISPECTRUM: AN EOR AND 21 CM-[CII]-[CII] CASE STUDY

ANGUS BEANE¹ & ADAM LIDZ¹*Draft version October 25, 2018*

ABSTRACT

The amplitude of redshifted 21 cm fluctuations during the Epoch of Reionization (EoR) is expected to show a distinctive “rise and fall” behavior with decreasing redshift as reionization proceeds. On large scales ($k \lesssim 0.1 \text{ Mpc}^{-1}$) this can mostly be characterized by evolution in the product of the mean 21 cm brightness temperature and a bias factor, $\langle T_{21} \rangle b_{21}(z)$. This quantity evolves in a distinctive way that can help in determining the average ionization history of the intergalactic medium (IGM) from upcoming 21 cm fluctuation data sets. Here we consider extracting $\langle T_{21} \rangle b_{21}(z)$ using a combination of future redshifted 21 cm and [CII] line-intensity mapping data sets. Our method exploits the dependence of the 21 cm-[CII]-[CII] cross-bispectrum on the shape of triangle configurations in Fourier space. This allows one to determine $\langle T_{21} \rangle b_{21}(z)$ yet, importantly, is less sensitive to foreground contamination than the 21 cm auto-spectrum, and so can provide a valuable cross-check. We compare the results of simulated bispectra with second-order perturbation theory: on the largest scales well-probed by our simulations ($k \sim 0.05 \text{ Mpc}^{-1}$), the perturbative estimate of $\langle T_{21} \rangle b_{21}$ matches the true value to within 10% for $\langle x_i \rangle \lesssim 0.8$. The perturbative formula is most accurate early in the EoR. We consider the 21 cm auto-bispectrum and show that this statistic may also be used to extract the 21 cm bias factor. Finally, we discuss the survey requirements for measuring the cross-bispectrum. Although we focus on the 21 cm-[CII]-[CII] bispectrum during reionization, our method may be of broader interest and can be applied to any two fields throughout cosmic history.

Subject headings: cosmology: theory – intergalactic medium – large scale structure of universe

1. INTRODUCTION

Observations of the redshifted 21 cm line promise to reveal the timing and spatial structure of the Epoch of Reionization (EoR) in the near future. This will help determine the formation time and properties of the first stars, galaxies, and accreting black holes, and the nature of large-scale structure at high redshift (Loeb & Furlanetto 2013). In order to understand the full astrophysical implications of the upcoming data, a range of challenges must first be overcome, both to mitigate systematic effects from foreground contamination and instrumental artifacts, and to faithfully model and interpret the measurements.

One goal of redshifted 21 cm surveys is to measure the redshift evolution of the power spectrum of 21 cm fluctuations. On large scales, the amplitude of the 21 cm power spectrum is expected to rise and fall with decreasing redshift as reionization proceeds (e.g. Lidz et al. 2008). This can in turn be used to extract information about the volume-averaged ionization fraction and its redshift evolution. On scales larger than the size of the ionized bubbles, this redshift evolution should mostly be characterized by a bias factor, $b_{21}(z)$, relating the 21 cm fluctuations to fluctuations in the underlying matter density field on large scales (Furlanetto et al. 2004), and by the spatial average 21 cm brightness temperature $\langle T_{21} \rangle(z)$. The bias factor description, if accurate, has the important virtue of providing a model-independent characterization of the 21 cm fluctuation measurements. The measured bias factors can then be compared with simulations

to extract information about the ionizing sources and the reionization history.

In conjunction with the 21 cm experiments, a number of efforts are underway to carry out line-intensity mapping surveys of the EoR in various other emission lines, such as [CII] (Crites et al. 2014), CO (Chung et al. 2017), and Ly α (Doré et al. 2016). In these line-intensity mapping observations, one measures the spatial fluctuations in the collective emission from many individually unresolved sources (Kovetz et al. 2017). Like the 21 cm experiments, these observations span large regions on the sky and provide accurate redshift information, enabling cross-correlation measurements with the 21 cm data sets (Lidz et al. 2011; Gong et al. 2012, 2011; Silva et al. 2015). Surveys in lines such as [CII] and CO should trace large-scale structure in the galaxy distribution and complement the redshifted 21 cm experiments, which probe the IGM (Lidz et al. 2009). (Ly α provides a useful intermediate case, reflecting fluctuations in both the source distribution and that of neutral hydrogen in the IGM, e.g. Pullen et al. 2014.) In addition, the line-intensity 21 cm cross-correlation is less susceptible to foreground contamination and other systematic effects than the auto-spectrum extracted from either data set alone (Furlanetto & Lidz 2007; Lidz et al. 2009; Lidz et al. 2011). The advantage of the cross-spectrum is that residual 21 cm foregrounds from galactic synchrotron, for example, may produce a strong bias in the auto-spectrum yet do not correlate on average with other tracers of high redshift structure.

Here we consider an approach for extracting $\langle T_{21} \rangle b_{21}(z)$ from a combination of line-intensity mapping and redshifted 21 cm data. Our aim is to develop a way of extracting this key quantity from upcoming data that

abeane@sas.upenn.edu

¹ Department of Physics & Astronomy, University of Pennsylvania, 209 South 33rd Street, Philadelphia, PA 19104, USA

is less susceptible to systematic contamination than the usual 21 cm auto-spectrum measurements. In this work we focus on the [CII] line, since surveys are already underway to detect this line from the EoR (Crites et al. 2014; Lagache 2017), but related measurements could be carried out using other lines.

The method developed here exploits the fact that the growth of large-scale structure under gravity generates non-Gaussianity, and that the resulting matter bispectrum has a distinctive dependence on triangle configuration. In the context of galaxy surveys, this has long been recognized and used to constrain galaxy bias (e.g. Fry 1994; Matarrese et al. 1997; Scoccimarro et al. 2001; Verde et al. 2002). In principle, a closely related measurement may be used to constrain 21 cm biasing as recently discussed by Hoffmann et al. (2018) in the context of the three-point correlation of the 21 cm field in configuration space. This recent work follows a number of papers on the general theme of using the 21 cm bispectrum to complement 21 cm power spectrum measurements during reionization (Bharadwaj & Pandey 2005; Shimabukuro et al. 2016, 2017; Majumdar et al. 2018). In addition to their utility in constraining 21 cm biasing, higher-order statistics are required to access the full information content of the highly non-Gaussian 21 cm signal expected during reionization.

Here we consider a variant of the usual approach for constraining biasing: we propose to extract $\langle T_{21} \rangle b_{21}(z)$ from a cross-bispectrum statistic, specifically the 21 cm-[CII]-[CII] bispectrum (involving one 21 cm field and two [CII] fields). This statistic has the virtue that it is less sensitive to foreground contamination than the 21 cm auto-spectrum and the 21 cm auto-bispectrum (for similar reasons to the two-point cross-correlation), and can potentially provide a powerful cross-check of inferences from the 21 cm auto-spectrum. We also consider extracting $\langle T_{21} \rangle b_{21}(z)$ from the 21 cm auto-bispectrum, and we find that this provides another route for constraining 21 cm biasing, in broad agreement with earlier work from Hoffmann et al. (2018). In contrast to this previous study, we work in Fourier space since this is a more natural basis for the interferometric 21 cm measurements. The 21 cm auto-bispectrum is, however, more sensitive to foreground contamination than the cross-bispectrum advocated here. On the other hand, it is likely a better probe of reionization's early phases since [CII] emission may be dim at early times, i.e. before metal enrichment is well underway.

The outline of this paper is as follows. In § 2 we present our approach for measuring the redshift evolution of the 21 cm bias factor. In § 3 we discuss the reionization simulations used to develop and test our analysis technique and the algorithm used to measure the bispectrum from simulations. We then discuss the simulated cross-bispectrum measurements in § 4, and consistency tests of the perturbative framework in § 5. In § 6 we discuss the prospects for measuring the cross-bispectra from future surveys. We summarize our results in § 7. We assume a Λ CDM cosmology, parameterized by $(\Omega_m, \Omega_\Lambda, \Omega_b, h, \sigma_8, n_s) = (0.27, 0.73, 0.046, 0.7, 0.8, 1)$, in broad consistency with recent Planck measurements (Planck Collaboration et al. 2016a)

2. CONSTRAINING 21 CM BIAS WITH THE CROSS-BISPECTRUM

Here we explain our technique, describing how the 21 cm bias may be extracted from the 21 cm-[CII]-[CII] cross-bispectrum. Consider first the 21 cm brightness temperature field, which describes the brightness temperature contrast between a neutral hydrogen cloud and the cosmic microwave background:

$$T_{21}(\mathbf{x}) = T_0 X_{\text{HI}}(\mathbf{x}) [1 + \delta_\rho(\mathbf{x})], \quad (1)$$

Here $T_0 = 28.1745 \text{ mK} [(1+z)/10]^{1/2}$ (e.g. Zaldarriaga et al. 2004), $X_{\text{HI}}(\mathbf{x})$ is the neutral hydrogen fraction (at position \mathbf{x}), and $\delta_\rho(\mathbf{x})$ is the gas density contrast, which is assumed to follow the overall matter density field on the large scales of interest. We can further define the fractional 21 cm brightness temperature fluctuation, $\delta_{21}(\mathbf{x}) = (T_{21}(\mathbf{x}) - \langle T_{21} \rangle) / \langle T_{21} \rangle$. Since $\langle T_{21} \rangle$ is not directly observable in an interferometric measurement, we will ultimately work with the statistics of $T_{21}(\mathbf{x})$, or more precisely its Fourier counterpart, $T_{21}(\mathbf{k})$.² However, it is cleaner to work with dimensionless fluctuation fields, such as $\delta_{21}(\mathbf{x})$, in describing biasing relations. Eq. 1 ignores the impact of peculiar velocities and spin temperature fluctuations, but these should be good approximations during most of the EoR (e.g. Jensen et al. 2013; Pritchard & Furlanetto 2007).

Similarly, we can consider the spatial fluctuations in the [CII] emission field, as probed by upcoming [CII] line-intensity mapping experiments. The [CII] emission is generally characterized by the three-dimensional specific intensity field, denoted here by $I_{\text{CII}}(\mathbf{x})$ (Lidz et al. 2011; Kovetz et al. 2017), or its Fourier partner, $I_{\text{CII}}(\mathbf{k})$. The fractional fluctuations in the [CII] specific intensity field are $\delta_{\text{CII}}(\mathbf{x}) = (I_{\text{CII}}(\mathbf{x}) - \langle I_{\text{CII}} \rangle) / \langle I_{\text{CII}} \rangle$.

As we will test subsequently using simulations of the EoR, we assume that on large scales each of these fluctuation fields is a deterministic and local function of the underlying matter density distribution (Scherrer & Weinberg 1998; Dekel & Lahav 1999). For example, we suppose that $\delta_{21}(\mathbf{x}) = f[\delta_\rho(\mathbf{x})]$, where f is the biasing function that specifies the relation between the 21 cm and matter density fluctuations. It is not obvious that the local biasing assumption is adequate for describing 21 cm fluctuations during reionization, since distant sources may impact the ionization state of the gas – especially at the late stages of reionization. However, as we will quantify, local biasing may nevertheless be a good approximation if we consider sufficiently large scales. Considering such scales, we Taylor expand the biasing function for small $\delta_\rho(\mathbf{x})$, keeping terms to second-order in the density fluctuations:

$$\delta_{21}(\mathbf{x}) = b_{21} \delta_\rho(\mathbf{x}) + \frac{b_{21}^{(2)}}{2} \delta_\rho^2(\mathbf{x}). \quad (2)$$

This equation defines the first-order and second-order 21 cm bias factors, b_{21} and $b_{21}^{(2)}$. (For brevity of notation, we do not include a super-script ⁽¹⁾ in our notation for the first-order bias factors.) The Fourier space coun-

² Our Fourier convention is: $T_{21}(\mathbf{k}) = \int d^3x T_{21}(\mathbf{x}) e^{i\mathbf{k}\cdot\mathbf{x}}$ and $T_{21}(\mathbf{x}) = \int \frac{d^3k}{(2\pi)^3} T_{21}(\mathbf{k}) e^{-i\mathbf{k}\cdot\mathbf{x}}$.

terpart of Eq. 2 is,

$$\delta_{21}(\mathbf{k}) = b_{21}\delta_\rho(\mathbf{k}) + \frac{b_{21}^{(2)}}{2} \int \frac{d^3q}{(2\pi)^3} \delta_\rho(\mathbf{q})\delta_\rho(\mathbf{k}-\mathbf{q}), \quad (3)$$

i.e. the $\delta_\rho^2(\mathbf{x})$ term in configuration space becomes a convolution in Fourier space. In practice, since $\langle T_{21} \rangle$ is not directly observable in an interferometric measurement, we generally consider the bias factors multiplied by $\langle T_{21} \rangle$. Under the assumption of a local and deterministic biasing relation for the [CII] specific intensity field, we define analogous bias factors b_{CII} and $b_{\text{CII}}^{(2)}$.

As large-scale structure grows under gravity, the matter density field will develop non-Gaussianity. At second-order in perturbation theory, the density fluctuations $\delta_\rho(\mathbf{k})$ follow (e.g. Bernardeau et al. 2002):

$$\delta_\rho(\mathbf{k}) = \delta_\rho^{(1)}(\mathbf{k}) + \int \frac{d^3q}{(2\pi)^3} F_2(\mathbf{q}, \mathbf{k}-\mathbf{q}) \delta_\rho^{(1)}(\mathbf{q}) \delta_\rho^{(1)}(\mathbf{k}-\mathbf{q}), \quad (4)$$

where $\delta_\rho^{(1)}$ denotes the first-order fluctuation field and $F_2(\mathbf{k}_1, \mathbf{k}_2)$ describes mode-coupling from non-linear growth. In a flat Λ CDM universe with $\Omega_m(z) \approx 1$, appropriate for high redshifts, the mode-coupling kernel is given by:

$$F_2(\mathbf{q}_1, \mathbf{q}_2) = \frac{5}{7} + \frac{\mathbf{q}_1 \cdot \mathbf{q}_2}{2q_1q_2} \left(\frac{q_1}{q_2} + \frac{q_2}{q_1} \right) + \frac{2}{7} \left(\frac{\mathbf{q}_1 \cdot \mathbf{q}_2}{q_1q_2} \right)^2. \quad (5)$$

This mode-coupling sources the matter density bispectrum, which is defined by:

$$\langle \delta_\rho(\mathbf{k}_1) \delta_\rho(\mathbf{k}_2) \delta_\rho(\mathbf{k}_3) \rangle \equiv (2\pi)^3 \delta_D(\mathbf{k}_1 + \mathbf{k}_2 + \mathbf{k}_3) \times B_{\delta,\delta,\delta}(\mathbf{k}_1, \mathbf{k}_2, \mathbf{k}_3). \quad (6)$$

Using the result of second-order perturbation theory, Eqs. 4 and 5 gives the bispectrum to lowest non-vanishing order as:

$$B_{\delta,\delta,\delta}^{(0)}(\mathbf{k}_1, \mathbf{k}_2, \mathbf{k}_3) = 2F_2(\mathbf{k}_1, \mathbf{k}_2) P_{\delta,\delta}^{\text{lin}}(k_1) P_{\delta,\delta}^{\text{lin}}(k_2) + 2 \text{ perm.}, \quad (7)$$

where $P_{\delta,\delta}^{\text{lin}}$ is the linear matter auto-spectrum and 2 perm. indicates permutations of the products of power spectra that enter, with each permutation picking out a product of two of the three wavevectors involved. We make a distinction here between the linear and nonlinear matter power spectra, but there is only a $\sim 5\%$ difference between the two for the smallest scales ($k \sim 0.4 \text{ Mpc}^{-1}$) and lowest redshift ($z \sim 6$) we consider. Since $B \propto P^2$, it is also convenient to define the reduced bispectrum. In the case of the matter density field,

$$Q_{\delta,\delta,\delta}(\mathbf{k}_1, \mathbf{k}_2, \mathbf{k}_3) = \frac{B_{\delta,\delta,\delta}(\mathbf{k}_1, \mathbf{k}_2, \mathbf{k}_3)}{P_{\delta,\delta}^{\text{nl}}(k_1) P_{\delta,\delta}^{\text{nl}}(k_2) + 2 \text{ perm.}}. \quad (8)$$

It is common to specify Q by the magnitude of wavevectors, $k_1 = |\mathbf{k}_1|$, and $k_2 = |\mathbf{k}_2|$, and the angle between \mathbf{k}_1 and \mathbf{k}_2 , θ_{12} .³ The reduced matter bispectrum has a distinctive form: first, gravitational mode-coupling (Eqs. 4-8) enhances the small-scale power spectrum in large-scale

³ We will use a different Fourier space characterization when we actually extract b_{21} from our simulations, see § 3.4

overdense regions compared to that in underdense regions. Second, the reduced bispectrum is smaller for triangles that are close to isosceles with $\theta_{12} \sim \pi/2$, than for triangles that are nearly co-linear with $\theta_{12} \sim 0, \pi$. This is a consequence of the filamentary nature of large-scale structure, and leads to a characteristic “U”-shaped dependence of $Q_{\delta,\delta,\delta}$ on θ_{12} (e.g. Bernardeau et al. 2002).

Turning to biased-tracers, such as the 21 cm or [CII] fluctuations, it is clear that (at lowest non-vanishing order) the bispectra of these fields receive contributions both from non-Gaussianity in the matter distribution (described by Eq. 8) and owing to non-linearities in the biasing relation (Eqs. 2-3). Here we consider the cross-bispectrum between the 21 cm field and two copies of the [CII] fluctuation field. This quantity is less sensitive to foreground contamination – and to unshared systematics – than the auto-bispectra of these fields. This is because the foregrounds in the two surveys should be mostly uncorrelated (asides for common foregrounds at the widely separated observing frequencies of the two experiments), and so should not contribute to the ensemble-averaged cross-bispectrum.⁴ Foreground cleaning or avoidance is still important because residual foregrounds will increase the variance of a cross-bispectrum estimate, but the cross-bispectrum has the important virtue that unshared foregrounds will not produce a spurious signal *on average*. The cross-power spectrum is also less sensitive to foreground contamination; however on large scales, the cross-spectrum is proportional to the overall product $b_{21} \langle T_{21} \rangle b_{\text{CII}} \langle I_{\text{CII}} \rangle$. That is, the cross-power spectrum depends on both the 21 cm and [CII] biasing relations, as well as the mean intensity in each line. On the other hand, we will show that the shape of the cross-bispectrum – when suitably defined – is sensitive only to $\langle T_{21} \rangle b_{21}$ (and independent of the [CII] biasing and mean intensity).

Specifically, consider the cross-bispectrum between a single 21 cm field and two [CII] emission fields:

$$\langle T_{21}(\mathbf{k}_1) I_{\text{CII}}(\mathbf{k}_2) I_{\text{CII}}(\mathbf{k}_3) \rangle \equiv (2\pi)^3 \delta_D(\mathbf{k}_1 + \mathbf{k}_2 + \mathbf{k}_3) \times B_{21,\text{CII},\text{CII}}(\mathbf{k}_1, \mathbf{k}_2, \mathbf{k}_3). \quad (9)$$

Note that we have now switched from considering δ_{21} and δ_{CII} to T_{21} and I_{CII} , since only the latter quantities are directly observable from interferometric and line-intensity mapping measurements. Apart from the overall $\mathbf{k} = 0$ mode, $T_{21}(\mathbf{k}) = \langle T_{21} \rangle \delta_{21}(\mathbf{k})$, and $I_{\text{CII}}(\mathbf{k}) = \langle I_{\text{CII}} \rangle \delta_{\text{CII}}(\mathbf{k})$.

We can define a reduced cross-bispectrum that is formed from Eq. 9 and the cross-power spectrum between the 21 cm and [CII] fields, $P_{21,\text{CII}}(k_i)$, at each of the three wavevectors k_i with $i = 1, 2, 3$. Specifically,

$$\hat{Q}_{21,\text{CII},\text{CII}}(\mathbf{k}_1, \mathbf{k}_2, \mathbf{k}_3) = \frac{B_{21,\text{CII},\text{CII}}(\mathbf{k}_1, \mathbf{k}_2, \mathbf{k}_3)}{P_{21,\text{CII}}(k_1) P_{21,\text{CII}}(k_2) + 2 \text{ perm.}} \quad (10)$$

⁴ Any correlations between the signal in one survey and the foregrounds in the other could also produce a small ensemble-averaged cross-bispectrum. For example, the high redshift [CII] emitting galaxies – or other correlated sources at the redshift of these galaxies – may emit synchrotron radiation which constitutes a (very small) “foreground” for the 21 cm survey.

Note that we deliberately construct the reduced cross-bispectrum using only the cross-power spectrum in the denominator of Eq. 10: explicitly, “2 perm.” is specified by $P_{21,\text{CH}}(k_2)P_{21,\text{CH}}(k_3) + P_{21,\text{CH}}(k_3)P_{21,\text{CH}}(k_1)$ and does not involve the auto-power spectrum of either field. Similar definitions hold for $\hat{Q}_{\text{CH},21,\text{CH}}$ and $\hat{Q}_{\text{CH},\text{CH},21}$; these merely rearrange which wavevector is attached to the 21 cm field. Note that with this definition, using mK units for T_{21} and Jy/str units for I_{CH} , the cross-bispectrum $B_{21,\text{CH},\text{CH}}$ has units of $\text{mK}(\text{Jy/str})^2(\text{Mpc})^6$, while the reduced cross-bispectrum $\hat{Q}_{21,\text{CH},\text{CH}}$ has units of mK^{-1} .

$$\begin{aligned}\hat{Q}_{21,\text{CH},\text{CH}}(\mathbf{k}_1, \mathbf{k}_2, \mathbf{k}_3) &= \frac{Q_{\delta,\delta,\delta}(\mathbf{k}_1, \mathbf{k}_2, \mathbf{k}_3)}{\langle T_{21} \rangle b_{21}} \\ &+ \frac{b_{21}^{(2)}}{2\langle T_{21} \rangle b_{21}^2} L(k_1, k_2) \\ &+ \frac{b_{\text{CH}}^{(2)}}{2\langle T_{21} \rangle b_{21} b_{\text{CH}}} [L(k_2, k_3) + L(k_3, k_1)],\end{aligned}$$

where we have defined

$$L(k_i, k_j) = \frac{P_{1,2}(k_i)P_{1,2}(k_j)}{P_{1,2}(k_1)P_{1,2}(k_2) + 2 \text{ perm.}}. \quad (11)$$

As will become clear shortly, these L terms are inconvenient, but note that

$$L(k_1, k_2) + L(k_2, k_3) + L(k_3, k_1) = 1. \quad (12)$$

Therefore, summing permutations of Eq. 2 and using Eq. 12 rids us of the L terms:

$$Q_{21,\text{CH},\text{CH}} \equiv \frac{1}{3} \left(\hat{Q}_{21,\text{CH},\text{CH}} + \hat{Q}_{\text{CH},21,\text{CH}} + \hat{Q}_{\text{CH},\text{CH},21} \right). \quad (13)$$

Throughout we will only work with $Q_{1,2,2}$, and so these permutations are implicit in what follows. Note that the permutations in Eq. 13 imply that swapping any two of the wavevector arguments results in the same value of Q . Therefore, we will also implicitly enforce $k_1 \geq k_2 \geq k_3$ where relevant, to avoid double counting.

With these permutations in mind, we now have the following formula:

$$\begin{aligned}Q_{21,\text{CH},\text{CH}} &= \frac{Q_{\delta,\delta,\delta}}{\langle T_{21} \rangle b_{21}} + \frac{1}{6} \frac{b_{21}^{(2)}}{\langle T_{21} \rangle b_{21}^2} \\ &+ \frac{1}{3} \frac{b_{\text{CH}}^{(2)}}{\langle T_{21} \rangle b_{21} b_{\text{CH}}}.\end{aligned} \quad (14)$$

As we have described, this formula is valid at second-order in perturbation theory. In our actual analysis, we will use the simulated $Q_{\delta,\delta,\delta}$ instead of the perturbative $Q_{\delta,\delta,\delta}$. This is mostly to minimize the impact of sample variance and is discussed further in § 4.

Our analysis strategy is now clear, and analogous to methods developed previously to constrain galaxy bias (Fry 1994; Matarrese et al. 1997; Scoccimarro et al. 2001; Verde et al. 2002). The first term in $Q_{21,\text{CH},\text{CH}}$ depends on the reduced density bispectrum, with its distinctive “U”-shaped dependence on θ_{12} , and the 21 cm linear bias factor. In this term, only the 21 cm bias enters and so this term is entirely independent of the statistical properties

of the [CII] emission fluctuations. In contrast, the other terms depend on the first and second-order bias factors of both the 21 cm and [CII] fields, and so these factors are harder to interpret, but produce only a constant offset. The rationale for taking the permuted version (Eq. 13) is now clarified, since as a result the [CII] bias factors enter only as an overall constant, independent of triangular configuration. In summary, by measuring the triangular shape dependence of $Q_{21,\text{CH},\text{CH}}$, we should be able to extract $\langle T_{21} \rangle b_{21}$.

In testing the perturbative framework described above, we will consider various additional bispectra. At lowest non-vanishing order in perturbation theory, these all have the general form:

$$Q_{21,\text{X},\text{X}}^{(0)} = \frac{Q_{\delta,\delta,\delta}}{\langle T_{21} \rangle b_{21}} + C_{21,\text{X},\text{X}}, \quad (15)$$

where the various values of C depend on which field “X” is being combined with the 21 cm fluctuations. Specifically,

$$C_{21,21,21} = \frac{1}{2} \frac{b_{21}^{(2)}}{\langle T_{21} \rangle b_{21}^2}, \quad (16)$$

$$C_{21,\delta,\delta} = \frac{1}{6} \frac{b_{21}^{(2)}}{\langle T_{21} \rangle b_{21}^2}, \quad (17)$$

and

$$C_{21,\text{CH},\text{CH}} = \frac{1}{6} \frac{b_{21}^{(2)}}{\langle T_{21} \rangle b_{21}^2} + \frac{1}{3} \frac{b_{\text{CH}}^{(2)}}{\langle T_{21} \rangle b_{21} b_{\text{CH}}}. \quad (18)$$

3. REIONIZATION SIMULATIONS AND METHODOLOGY

In order to characterize the cross-bispectrum signal at different stages of reionization, and to test the accuracy of the perturbative formulas from the previous section, we turn to semi-numerical simulations of the EoR (Zahn et al. 2006; Mesinger & Furlanetto 2007), based on the excursion-set (Bond et al. 1991) model of reionization (Furlanetto et al. 2004). Specifically, we use the publicly available 21cmFAST code v1.12 (Mesinger et al. 2011).

Our simulations are unlikely to provide fully accurate models of the small-scale 21 cm signal. In the context of this paper, the small-scale modes mostly set the overall values of the bias factors ($\langle T_{21} \rangle b_{21}$) at different redshifts and neutral fractions. The small-scale modes should therefore impact the precise evolution of the bias factors with redshift, and not the overall framework we propose here.

3.1. L-PICOLA

By default, 21cmFAST uses the Zel’dovich approximation (ZA) to generate the density field (Zel’dovich 1970). This is appropriate for capturing the large-scale two-point statistics of the 21 cm field at high redshifts, but it is inadequate for modeling three-point statistics. The ZA is known to underestimate the density bispectrum (Scoccimarro 1997; Leclercq et al. 2013), and we have verified that it provides a poor description of the density bispectrum at the scales and redshifts of interest for our study. We thus turn to the publicly available L-PICOLA v1.3 code (Howlett et al. 2015; Tashev et al. 2013), which is a hybrid between a 2nd order Lagrangian perturbation theory (2LPT) and a particle mesh (PM) code. L-PICOLA

is a parallel version of the COLA method, and accurately reproduces the two and three-point statistics of interest of our study, yet is less computationally expensive than full GADGET-2 (Springel 2005) runs.

In order to accurately estimate the bispectra starting at $z \sim 10.5$, two potential issues are: transients associated with the initial conditions (Crocce et al. 2006) and discreteness noise from the finite number of particles in the simulation. These issues are more of a concern at the high redshifts of interest for our study (than near $z = 0$), since there is less time for transients to relax and because the density fluctuations are small at early times. The transients are suppressed in part by adopting 2LPT initial conditions (as opposed to Zel’dovich initial conditions) and by starting the simulation early. We guard against shot-noise by simulating a fairly high particle density. Specifically, we simulate 1024^3 particles in a simulation box with a co-moving side length of $L_{\text{box}} = 800 \text{ Mpc}$. We chose an extremely high starting redshift of $z_i = 5000$.⁵ The code takes 300 time steps between z_i and $z = 10.49$.

In order to beat-down noise in our bispectrum estimates on large scales, we run ten different realizations of the L-PICOLA simulations, resulting in a total simulated volume of 5.12 Gpc^3 . The boxsize was chosen so that the fundamental mode of the simulation box is much larger than the scales of interest for our study. Specifically, the largest scale considered is $k = 0.05 \text{ Mpc}^{-1}$ and the fundamental mode of the simulation box is $k_f = 0.00785 \text{ Mpc}^{-1}$. We save simulation snapshots at redshifts of $z = 10.49, 9.41, 8.43, 7.88, 7.37, 7.05, 6.73, 6.43$, and 6.00 , and take ten time steps between each output. For each redshift snapshot, we use nearest grid-point interpolation to estimate the density field on a 512^3 Cartesian grid from the particle positions.

3.2. 21cmFAST

The 512^3 particle, $L_{\text{box}} = 800 \text{ Mpc}$, gridded density fields from the L-PICOLA runs are then passed to the 21cmFAST code to generate simulated ionization and 21 cm fields at each redshift. Specifically, the excursion set approach is used to identify ionized regions (Mesinger et al. 2011) using the following simulation parameters: the ionizing efficiency is set to $\zeta = 10$, the minimum virial temperature of galaxy hosting halos is $T_{\text{vir}} = 10^4 \text{ K}$; the largest smoothing scale – for generating the ionization field using the excursion-set methodology – is $R_{\text{max}} = 30$ co-moving Mpc. (The latter quantity is sometimes loosely termed the “mean-free path”, R_{mfp} , in the literature.)

The *Top panel* of Fig. 1 shows the redshift evolution of the volume-averaged neutral fraction, $\langle x_{\text{HI}} \rangle$, in our 21cmFAST model. In this model, reionization completes shortly after $z \sim 6$, while 50% of the volume is ion-

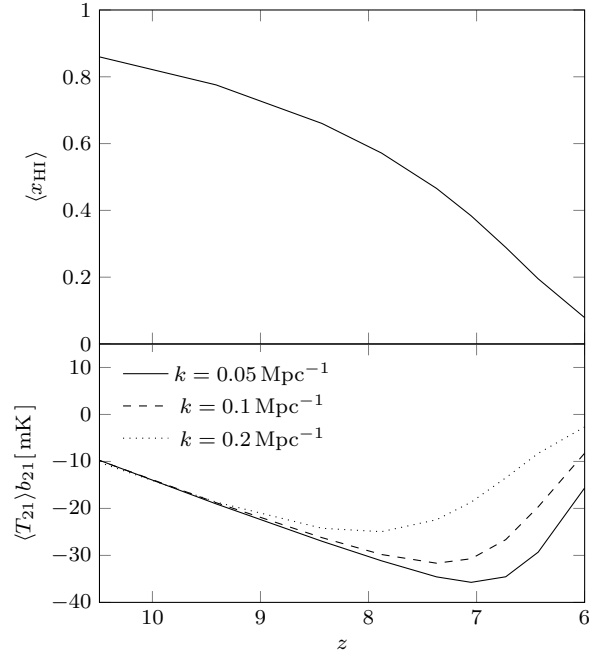


FIG. 1.— The ionization history and the redshift evolution of the 21 cm bias factor. *Top panel:* The volume-averaged neutral hydrogen fraction, $\langle x_{\text{HI}} \rangle$, as a function of redshift from our 21cmFAST simulation. *Bottom panel:* The corresponding evolution of the 21 cm bias factor, $\langle T_{21} \rangle b_{21}$, which rises and falls with decreasing redshift and peaks (in amplitude) around reionization’s midpoint, when $\langle x_i \rangle \sim 0.5$ – or slightly thereafter – of the IGM volume is reionized. We compute $\langle T_{21} \rangle b_{21}$ from the 21 cm-density cross-spectrum at various k . At high redshifts (early in reionization) $\langle T_{21} \rangle b_{21}$ is insensitive to the precise wavenumber considered, but differences appear as reionization proceeds. This provides one indication of the redshifts and scales where the linear biasing description becomes imperfect.

ized at $z \sim 7.5$, and 20% is ionized by $z \sim 10$; this is broadly consistent with current constraints on the EoR (e.g. Becker et al. (2001); Fan et al. (2006); Venemans et al. (2013); Becker et al. (2015); Planck Collaboration et al. (2016b)). The *Bottom panel* shows the corresponding evolution of the 21 cm bias factor with redshift, $\langle T_{21} \rangle b_{21}$ (estimated from the 21 cm density cross-power spectrum as we detail subsequently) calculated at each of $k = 0.05 \text{ Mpc}^{-1}, 0.1 \text{ Mpc}^{-1}$, and 0.2 Mpc^{-1} . Fig. 1 exemplifies the distinctive “rise and fall” evolution in the magnitude of $\langle T_{21} \rangle b_{21}$: a key goal of upcoming 21 cm surveys is to measure this evolution, and to use it to extract the corresponding ionization history. Reiterating, the motivation of our paper is to develop an approach for extracting this evolution which is less susceptible to foreground contamination than the 21 cm auto spectrum. At early times, the bias factor inferred is identical for all three spatial scales considered. However, as reionization proceeds the bias factor starts to depend on wavenumber: this occurs because the ionized regions grow in size during reionization, and the linear biasing description breaks down on progressively larger scales. Hence, even on the rather large scales spanned by our simulation box we expect linear biasing to be an imperfect description during the late stages of reionization (as we will quantify further subsequently). In practice, it will probably be challenging to access still larger scales from future surveys (where linear biasing might be a better description), since foreground avoidance or cleaning limit the prospects for ex-

⁵ The starting redshift is artificially high; the initial conditions are set by rescaling from the $z = 0$ matter power spectrum assuming that the universe is dominated by pressure-free matter at the initial redshift (even though this redshift is formally before matter-radiation equality.) The subsequent evolution is tracked by L-PICOLA and this returns the correct linear evolution (under the approximation that the universe is entirely composed of pressure-free matter) after recombination. The early start was just meant to guard against initial transients and to ensure the correct density statistics at $z \sim 6 - 11$.

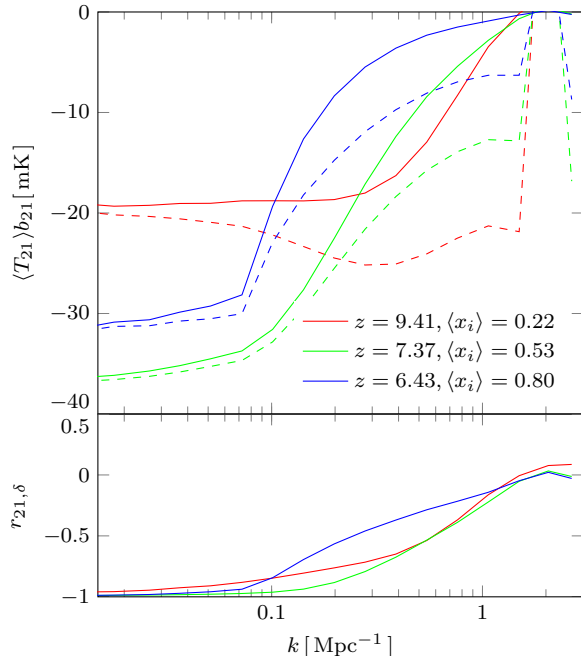


FIG. 2.— Linear biasing of the 21 cm fluctuations and its range of validity. *Top panel:* Estimates of the scale-dependent bias factor, $\langle T_{21} \rangle b_{21}(k)$, from our reionization simulation for several different redshifts and ionization fractions ($\langle x_i \rangle$), as described in the legend. The solid lines show estimates from the 21 cm auto-power spectrum, while the dashed lines show the bias factor inferred from the 21 cm-density cross-power spectrum. *Bottom panel:* The cross-correlation coefficient between the 21 cm and matter density fields, $r_{21,\delta}(k)$. At $k \lesssim 0.1 \text{ Mpc}^{-1}$, the bias factor is close to scale-independent, and $r_{21,\delta}(k) \sim -1$.

tracting very large scale modes. (See, e.g., Fig. 1 of Dillon et al. 2014 and the discussion therein.)

Lastly, note that the bias factor in the *Bottom panel* of Fig. 1 is *negative*: this indicates that large-scale overdense regions are dimmer in 21 cm emission than typical regions. The negative sign results because the ionizing sources form first in large-scale overdense regions and so these regions are ionized early. It is worth remarking that the 21 cm auto-power spectrum is sensitive only to $[\langle T_{21} \rangle b_{21}]^2$ and hence can not distinguish the overall sign here. On the other hand, the 21 cm-[CII] cross-spectrum, the 21 cm auto-bispectrum, and the 21 cm-[CII]-[CII] cross-bispectrum each depend on both the magnitude and the sign of $\langle T_{21} \rangle b_{21}$, as has also been shown by Majumdar et al. (2018); Hoffmann et al. (2018).

We can carry out further tests of the linear biasing approximation using additional two-point statistical measures. As already mentioned, we expect this approximation to break down on sufficiently small scales, especially during the later stages of reionization. On scales smaller than the size of the ionized regions, there are order unity fluctuations in the ionization fraction, as some areas in the IGM are nearly completely ionized while others remain almost completely neutral. In addition, the ionization and density field de-correlate on scales smaller than the size of the ionized bubbles (e.g. Furlanetto et al. 2004; Zahn et al. 2006). Hence on these scales, the 21 cm and density fluctuation fields do not share the same phases and an expansion along the lines of Eq. 2 is inadequate. To explore this we estimated the bias factor from the cross-power spectrum of the 21 cm and density

fields, $b_{21,x}(k) = P_{21,\delta}(k)/P_{\delta,\delta}(k)$, and from the 21 cm auto-power spectrum $b_{21,a}(k) = [P_{21,21}(k)/P_{\delta,\delta}(k)]^{1/2}$ (*Top panel* of Fig. 2). Note that these two estimates should agree in the linear-biasing regime, but may depart from each other on smaller scales (at higher k). Furthermore, we calculate the cross-correlation coefficient between the 21 cm and density fields, $r_{21,\delta}(k) = P_{21,\delta}(k)/\sqrt{P_{21,21}(k)P_{\delta,\delta}(k)}$ (*Bottom panel*). The cross-correlation coefficient quantifies how well the phases of the two fields track each other.

At $k \lesssim 0.1 \text{ Mpc}^{-1}$, for the redshifts shown: the correlation-coefficient between the two fields is $r_{21,\delta} \sim -1$, and the bias factor is fairly scale-independent. The auto/cross-power spectrum approaches for calculating the bias factor also agree with each other to within $\sim 20\%$ for $k \sim 0.1 \text{ Mpc}^{-1}$, and to within $\sim 5\%$ for $k \sim 0.05 \text{ Mpc}^{-1}$ at $\langle x_i \rangle = 0.8$ ($z = 6.43$). The linear biasing description appears best in the middle of reionization. Towards the end of reionization, as illustrated by the blue $\langle x_i \rangle = 0.80$ curves, the bubbles are large enough that $k \sim 0.1 \text{ Mpc}^{-1}$ is only marginally in the linear biasing regime. On the other hand, in the earliest phases of reionization ($\langle x_i \rangle \sim 0.1$), the correlation-coefficient departs significantly from $r_{21,\delta} \sim -1$: this likely results because the sign of $r_{21,\delta}$ is initially *positive* and gradually reverses (Lidz et al. 2008). This occurs because the large-scale overdense regions prior to reionization contain more neutral hydrogen and are brighter in 21 cm emission than underdense areas, while the large-scale overdense regions ionize first and subsequently become dimmer in 21 cm. In our model large-scale overdense and underdense regions are nearly at the same brightness temperature at $\langle x_i \rangle \sim 0.1$ while the reversal is almost complete by $\langle x_i \rangle = 0.22$ at $z = 9.41$ (the earliest case shown in Fig. 2). We do not expect our perturbative formula to be accurate in the brief earlier phase near $\langle x_i \rangle \sim 0.1$, where $r_{21,\delta}$ changes sign rapidly. Note also that we neglect spin temperature fluctuations, which should impact our predictions at early times. In general, however, our results suggest that linear biasing is a fairly good description at $k \lesssim 0.1 \text{ Mpc}^{-1}$ during the bulk of reionization, further motivating us to test our cross-bispectrum method.

3.3. [CII] Intensity Field

In order to model the [CII] intensity field, our simulations would ideally resolve halos with masses down to the atomic cooling limit ($\sim 10^8 M_\odot$). In this case, we could model the high redshift [CII] intensity field by assuming correlations between halo properties and [CII] luminosity. However, it is difficult to resolve such small mass halos while capturing a large enough volume to accurately model the bispectrum. For example, the particle mass in our simulations is $\sim 10^{10} M_\odot$ and so we don't resolve many of the small mass halos which may host [CII] emitting galaxies. Consequently, we defer a full treatment of [CII] emission to future work.

Note, however, that the perturbative formulae (Eq. 14 and Eq. 15) predict – apart from the overall constant term – that the $Q_{21,\text{CII},\text{CII}}$ bispectrum should be identical to that of the $Q_{21,\delta,\delta}$ bispectrum. That is, both of these cross-bispectra are expected to follow the $Q_{\delta,\delta,\delta}/(\langle T_{21} \rangle b_{21})$ form. Consequently, we study the statistics of $Q_{21,\delta,\delta}$ here rather than $Q_{21,\text{CII},\text{CII}}$ since the

latter is more difficult to model. The main shortcoming of this approach is that it neglects the additional non-linearities in the [CII] biasing relation, and these effects may reduce the agreement with the perturbative formula. In estimating the signal-to-noise ratio at which $Q_{21,\text{CII},\text{CII}}$ may be measured in future surveys (§ 6), we assume a linear biasing model for [CII] emission. This allows us to predict the [CII] auto-spectrum and [CII]-21 cm cross-spectrum (as required for the signal-to-noise ratio calculation) from the statistics of the simulated density field. It may be possible to construct a sub-grid model to include unresolved small halos with the correct statistical properties (e.g. McQuinn et al. (2007)). However, the approach adopted in that work would need to be extended to capture the correct quadratic halo bias and is beyond the scope of this paper.

3.4. Estimating the Bispectrum

In order to estimate the bispectrum from our 21cm-FAST simulation outputs, we follow the method described in Smith et al. (2008). Throughout we consider two characterizations of the wavevector arguments. In both cases we calculate the average bispectrum in linearly-spaced wavevector bins.

Our first characterization is for illustration purposes only. Here we fix the magnitude of $|\mathbf{k}_1|$ and $|\mathbf{k}_2|$ while varying the angle θ_{12} between the two wavevectors. The third side of the triangle, \mathbf{k}_3 , is determined by these three parameters and the requirement of translation invariance ($\mathbf{k}_1 + \mathbf{k}_2 + \mathbf{k}_3 = \mathbf{0}$.) We consider spherical bins around each wavevector of thickness $\Delta k = k_f$, where $k_f = 2\pi/L_{\text{box}} = 0.00785 \text{ Mpc}^{-1}$ is the fundamental mode of our simulation box.

Our second characterization sets a minimum (k_{\min}) and a maximum (k_{\max}) magnitude for each wavevector argument. That is, we enforce $k_{\min} < |\mathbf{k}_i| < k_{\max}$ for each wavevector \mathbf{k}_i , along with the usual constraint that $\mathbf{k}_1 + \mathbf{k}_2 + \mathbf{k}_3 = \mathbf{0}$. Owing to homogeneity and isotropy, all bispectra have three arguments: $|\mathbf{k}_1|, |\mathbf{k}_2|, |\mathbf{k}_3|$. Our bins are cubes of side length $4k_f$ in Fourier space. This characterization captures nearly all the available modes. As discussed in § 2, we also enforce that $k_1 \geq k_2 \geq k_3$. In estimating bispectra, we loop through all of the simulated Fourier modes that lie within this wavevector range. We determine $B_{21,\delta,\delta}$ and $P_{21,\delta}$ from the same set of Fourier modes to reduce sample variance in our estimates of $Q_{21,\delta,\delta}$. In general, one would like to make k_{\min} and k_{\max} as small and large as possible, respectively. However, our estimates at small k are noisy and the perturbative formula becomes less accurate at high k . We chose values of k_{\min} and k_{\max} throughout that give the best results, but also show results for different values of k_{\min} and k_{\max} in Appendix A.

4. RESULTS

First we consider the reduced auto-bispectrum of the simulated matter density field, $Q_{\delta,\delta,\delta}(\theta_{12})$, at the redshifts of interest in Fig. 3. As discussed in § 3.1, we average over ten independent simulation realizations. We show the simulated reduced density bispectrum for triangles with $k_1 = 0.1 \text{ Mpc}^{-1}$ and $k_2 = 2k_1$ and a case where the wavenumbers are twice as large. In the larger-scale case, the simulated bispectra are somewhat noisy

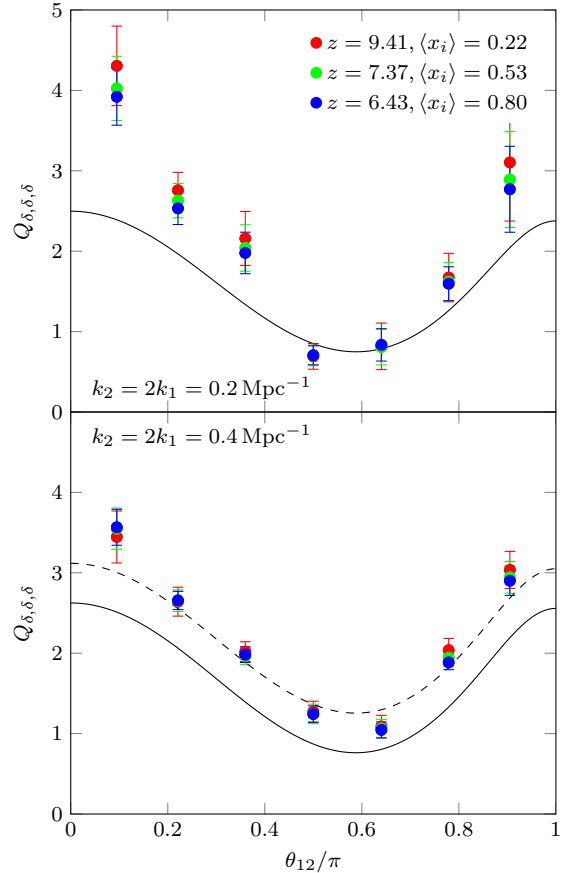


FIG. 3.— Reduced bispectrum of the density field. Here we fix $k_2 = 2k_1 = 0.2 \text{ Mpc}^{-1}$ in the *Upper panel* and $k_2 = 2k_1 = 0.4 \text{ Mpc}^{-1}$ in the *Bottom panel*. We plot the results as a function of θ_{12} , the angle between the two wavevectors. The solid line is the prediction of second-order perturbation theory, as given in Eq. 5. Each colored point shows the average reduced bispectrum from ten different simulation realizations. The error bars give estimates of the error on the average, as determined from the scatter across the ten simulation realizations. Note that the poorer sampling for nearly collinear triangle configurations leads to noisier estimates near $\theta_{12}/\pi \approx 0.1$. The dashed line is the perturbative $Q_{\delta,\delta,\delta}$ but with a constant added to minimize the χ^2 difference with the $z = 7.37$ measurements. This indicates that, for the most part, the perturbative $Q_{\delta,\delta,\delta}$ differs from the simulation results only by an overall constant.

while the smaller-scale case provides a smoother bispectrum estimate, because of the larger number of sampled modes at smaller scales. The simulation measurements are generally similar to the predictions of second order perturbation theory (Eq. 7) for the large scales shown and the high redshifts considered, although there are noticeable differences. The departures from the predictions of second-order perturbation theory evident in the figure reflect non-linearities that are not fully captured at second-order in δ . In order to partly account for these non-linear density fluctuations, we subsequently use the *simulated* density auto-bispectrum, $Q_{\delta,\delta,\delta}$, as input to the perturbative formulae (Eqs. 14 and 15). Throughout, we refer to this prediction loosely as the “second-order perturbation theory prediction” although strictly speaking it accounts for the impact of additional non-linearities in the form of $Q_{\delta,\delta,\delta}$. This also serves to reduce the impact of sample variance in our comparisons between simulations and perturbation theory estimates.

That being said, the departures from non-linearity manifest mainly as an overall constant. We illustrate this by showing in Fig. 3 (dashed line) the perturbative $Q_{\delta,\delta,\delta}$ but with a constant added to minimize the χ^2 statistic at $z = 7.37$. The agreement between the dashed line and the points at $k_2 = 2k_1 = 0.4 \text{ Mpc}^{-1}$ indicates that the non-linearities will propagate into $C_{21,X,X}$ but not into $\langle T_{21} \rangle b_{21}$. While this is not the case for the noisier $k_2 = 2k_1 = 0.2 \text{ Mpc}^{-1}$ panel, we nonetheless proceed with these caveats in mind.

We next consider the reduced 21 cm auto-bispectrum as a function of ionization fraction, along with the 21 cm- δ - δ cross-bispectrum.⁶ Our goals here are two-fold: first, we want to ascertain whether these quantities evolve strongly with $\langle x_i \rangle$, as expected if their evolution is driven, in part, by the “rise and fall” behavior illustrated in Fig. 1. Second, we aim to see if the simulated bispectra follow the perturbative expectation that $Q_{21,X,X} = Q_{\delta,\delta,\delta} / \langle T_{21} \rangle b_{21} + C_{21,X,X}$.

Fig. 4 shows that the various bispectra evolve strongly with ionization fraction. This is encouraging for our ultimate goal of using these measurements to extract information about the ionization history. The overall value and evolution of the reduced bispectra vary somewhat depending on which bispectrum is calculated, but this is expected since the values of $C_{21,21,21}$ and $C_{21,\delta,\delta}$ should differ by a factor of 3. Nevertheless, the overall shape of the two bispectra are similar, and the bispectra share the same ordering – from smallest to largest Q – with increasing ionization fraction.

In order to test the perturbative formula, we determine the best fit $\langle T_{21} \rangle b_{21}$ and $C_{21,X,X}$ for $Q_{21,X,X}$. To carry out these fits we use the variance estimated from the scatter across our ten simulation realizations. We neglect the covariance between different wavevector bins, since our estimates of the off-diagonal elements of the covariance matrix are too noisy to be reliable. We expect this to have relatively little impact on the best fit parameters, but it does prevent us from assessing the overall goodness of fit of the perturbative formula since the effective number of degrees of freedom are uncertain. The inability to measure covariance also prevents us from accurately computing error bars on the inferred $\langle T_{21} \rangle b_{21}$ and $C_{21,X,X}$. We defer this calculation to future studies.

5. CHECKING THE PERTURBATIVE FORMULAS

An interesting test of the perturbative framework is to compare the values of $\langle T_{21} \rangle b_{21}$ and $C_{21,X,X}$ inferred from a broad range of simulated two and three-point statistics. First, we compare the values of $\langle T_{21} \rangle b_{21}$ extracted from our fits to $Q_{21,X,X}$ with those from the 21 cm-density cross-power spectrum. The results of this comparison are shown for a range of ionization fractions in Fig. 5. In general, all three approaches return similar values of $\langle T_{21} \rangle b_{21}$ and share the same qualitative evolution with ionization fraction. However, the $\langle T_{21} \rangle b_{21}$ estimates from the cross-power spectrum and

the cross-bispectrum agree better with each other than with the auto-bispectrum inferences. This likely results because the 21 cm auto-bispectrum involves three significantly non-Gaussian fields (at least on scales smaller than the size of the ionized regions) and so our perturbative expansion is presumably less accurate for the auto-bispectrum. We find that by using $Q_{21,\delta,\delta}$, we are able to recover $\langle T_{21} \rangle b_{21}$ to within 5% for $\langle x_i \rangle < 0.5$, and 10% for $\langle x_i \rangle > 0.5$, except at the lowest redshift we tested ($z = 6$). On the other hand, $Q_{21,21,21}$ is only able to recover $\langle T_{21} \rangle b_{21}$ to within $\sim 20\%$ accuracy for all of the EoR, although the precise number quoted here may be subject to noise in our $Q_{21,21,21}$ estimates.

The agreement between the cross-power spectrum and cross-bispectrum estimates is best at $\langle x_i \rangle \lesssim 0.6$, at which point they separate a bit, before briefly coming together near $\langle x_i \rangle \sim 0.8$; they then split-off slightly again towards the tail-end of reionization. The results in Fig. 5 adopt triangles with wavevectors between $k_{\min} = 0.05 \text{ Mpc}^{-1}$ and $k_{\max} = 0.4 \text{ Mpc}^{-1}$. In Appendix A (Fig. 10) we investigate other choices for the range of wavevectors used in our fitting procedure. There we show that the values of $\langle T_{21} \rangle b_{21}$ inferred from $Q_{21,\delta,\delta}$ are insensitive to the precise choices of k_{\min} and k_{\max} , while the results from $Q_{21,21,21}$ are noisier and show more sensitivity to the choice of scales.

We can also test whether the constant offset terms agree with the formulas from perturbation theory (Eqs. 16-18). Before considering this test, we note that the behavior of the constant offset term with redshift may offer an additional handle on the ionization history since e.g. $C_{21,21,21}$ is a measurable quantity. Indeed, Fig. 6 shows that the constant offsets evolve fairly strongly with redshift/ionization fraction, and that the different offset terms evolve in qualitatively similar ways with average ionization fraction. However, note that $C_{21,\text{CII},\text{CII}}$, which is most robust to foreground contamination, depends on b_{CII} and $b_{\text{CII}}^{(2)}$; that is, this quantity depends on both the [CII] and the 21 cm biasing and is therefore more challenging to interpret.

The perturbative prediction (Eqs. 16 and 17) is that the constant offsets are related by $C_{21,21,21} = 3C_{21,\delta,\delta}$. Since we extracted each of these terms independently, we are able to test this statement without extracting $\langle T_{21} \rangle b_{21}^{(2)}$. We plot the ratio $C_{21,21,21}/3C_{21,\delta,\delta}$ in Fig. 7. It is encouraging that for the much of the reionization process this ratio lies within 10 – 20% of unity. The departures shown in the figure arise: i) at very early times (near $\langle x_i \rangle \sim 0.1$) when the correlation coefficient reverses sign (see §3.2), ii) near $\langle x_i \rangle \sim 0.7$ when each of the constant offset terms happen to be close to zero and sample variance likely impacts our estimate of this ratio, and iii) near the end of reionization when the ionized regions are large and the perturbative framework is expected to break down.

For completeness, we note that with more detailed [CII] emission models, one could carry out further tests of the perturbative framework. Specifically, the perturbative formulas demand specific relationships between the constant offset terms for the 21 cm-[CII]-[CII] cross-bispectrum, the 21 cm- δ - δ cross-bispectrum, the 21 cm auto-bispectrum, and the [CII] auto-bispectrum. Using Eqs. 15 - 18, and analogous formulas for the [CII] inten-

⁶ The 21 cm-[CII]-[CII] cross-bispectrum is ultimately the quantity of interest, but as discussed in § 3.3, we are unable to capture small mass halos and so we use the 21 cm- δ - δ bispectrum as a proxy for the 21 cm-[CII]-[CII] bispectrum. If the second-order predictions in § 2 are correct, then we expect that all three of these bispectra differ only by a redshift-dependent constant.

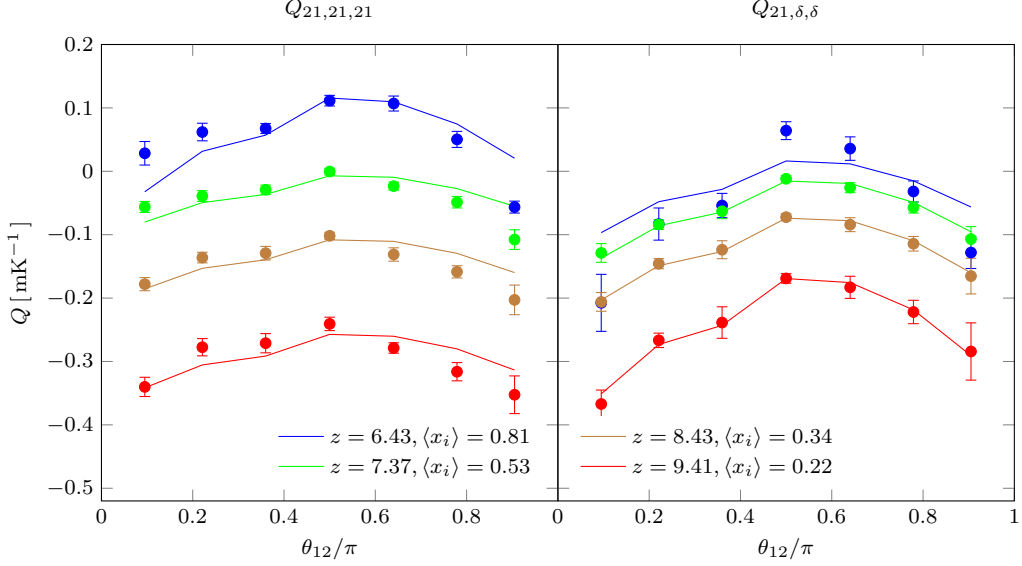


FIG. 4.— Evolution of various reduced bispectra with redshift/ionization fraction. *Left*: the reduced 21 cm auto-bispectrum. *Right*: the reduced 21 cm-density-density cross-bispectrum. In each panel, the solid lines show the best fit models of the form $Q_{\delta,\delta,\delta}/\langle T_{21} \rangle b_{21} + C$, using the simulated values of $Q_{\delta,\delta,\delta}$. We restrict ourself to modes that satisfy $k_1 = 0.1 \text{ Mpc}^{-1}$ and $k_2 = 0.2 \text{ Mpc}^{-1}$, varying the angle θ_{12} between the two wavevectors. Note that the best fit values of $\langle T_{21} \rangle b_{21}$ and C here are obtained by fitting only to this restricted range of triangle configurations and differ somewhat from the best fits obtained subsequently, which match to a broader range of triangles. The perturbative formula provides a better match to $Q_{21,\delta,\delta}$ than $Q_{21,21,21}$ as we discuss in the text. Note that since we use the simulated $Q_{\delta,\delta,\delta}$ in our fits, the curves share some of the noise in our simulation estimates.

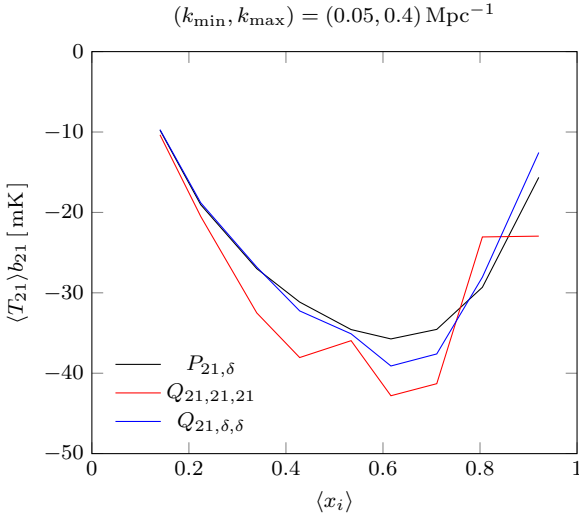


FIG. 5.— Consistency between different estimates of $\langle T_{21} \rangle b_{21}$. The black line show the linear 21 cm bias factor, $\langle T_{21} \rangle b_{21}$, inferred from the cross-power spectrum, $\langle T_{21} \rangle b_{21} = P_{21,\delta}/P_{\delta,\delta}$ at $k = 0.05 \text{ Mpc}^{-1}$, as a function of $\langle x_i \rangle$. These are compared with the linear bias inferred from $Q_{21,21,21}$ (red) and $Q_{21,\delta,\delta}$ (blue).

sity field, we have that,

$$\frac{3}{2} \frac{C_{21,\text{CII},\text{CII}} - C_{21,\delta,\delta}}{C_{\text{CII},\text{CII},\text{CII}}} = \frac{b_{\text{CII}}}{b_{21}} \quad (19)$$

and, similarly,

$$\frac{3}{2} \frac{C_{21,\text{CII},\text{CII}} - \frac{1}{3} C_{21,21,21}}{C_{\text{CII},\text{CII},\text{CII}}} = \frac{b_{\text{CII}}}{b_{21}}. \quad (20)$$

We comment in passing that another possibility is to extract $\langle I_{\text{CII}} \rangle b_{\text{CII}}$ from the analogous cross-bispectrum, $Q_{\text{CII},21,21}$. If line-intensity mapping experiments are performed using additional emission lines such as Ly- α or us-

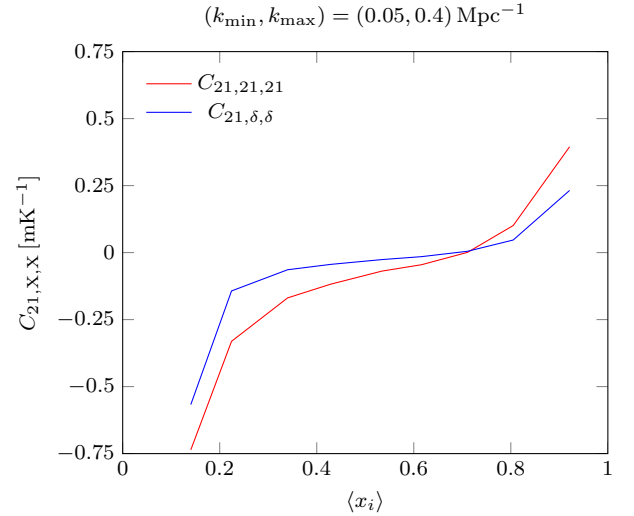


FIG. 6.— Evolution of the constant offset terms, $C_{21,X,X}$ with ionization fraction. Note that it appears that $C_{21,21,21} \sim C_{21,\delta,\delta}$ for $\langle x_i \rangle \sim 0.7$. This occurs, however, because both constant offset terms are very close to zero at this ionization fraction. See Fig. 7. ing rotational transitions from CO molecules, the cross-bispectra methodology may allow further inferences and consistency checks.

6. DETECTABILITY

We now discuss the prospects of measuring the 21 cm-[CII]-[CII] cross-bispectrum from future surveys. Here our aim is to obtain rough estimates of the joint sky coverage and noise power spectra required for upcoming [CII] and 21 cm surveys to detect this signal.

6.1. [CII] Statistics

As discussed in § 3.3, our current modeling assumes that the reduced cross-bispectrum $Q_{21,\text{CII},\text{CII}}$ tracks

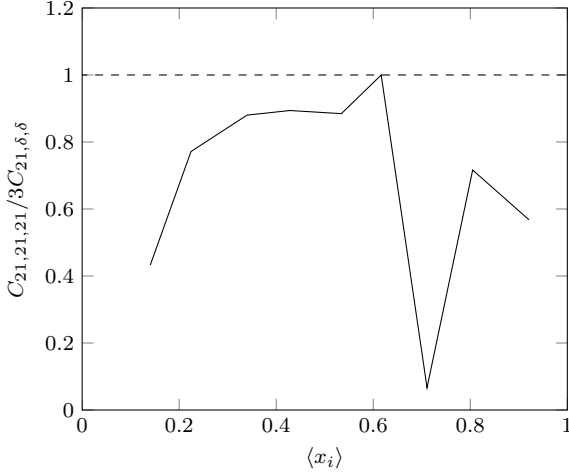


FIG. 7.— Consistency check on the constant offset terms. If second-order perturbation theory is accurate, we expect $C_{21,21,21}/3C_{21,\delta,\delta} = 1$. We find that this ratio is within 20% of unity during the bulk of reionization. The dip at $\langle x_i \rangle \sim 0.7$ results because $C_{21,21,21}, C_{21,\delta,\delta} \sim 0$: at this stage of reionization, more simulation realizations would be required to accurately estimate the ratio of these small values.

$Q_{21,\delta,\delta}$ apart for an overall constant. In order to calculate the variance of $Q_{21,\text{CII},\text{CII}}$, we require a model for the [CII] emission power spectrum and the cross-power spectrum with the 21 cm field. For this purpose, we assume a linear biasing model for the [CII] emission fluctuations:

$$\begin{aligned} P_{\text{CII},\text{CII}} &= (b_{\text{CII}} \langle I_{\text{CII}} \rangle)^2 P_{\delta,\delta} \\ P_{21,\text{CII}} &= b_{\text{CII}} \langle I_{\text{CII}} \rangle P_{21,\delta}. \end{aligned} \quad (21)$$

Here b_{CII} is the luminosity-weighted bias of the halos that host [CII]-emitting galaxies. For simplicity, we suppose that $b_{\text{CII}} = 3$ at all redshifts of interest; our results are relatively insensitive to this choice. We follow Lidz & Taylor (2016) (which is based on Lidz et al. (2011); Pullen et al. (2014)) in calculating $\langle I_{\text{CII}} \rangle$. Specifically, we assume a one-to-one mapping between star formation rate, SFR, and [CII] luminosity. The average specific intensity of the [CII] emission is:

$$\langle I_{\text{CII}} \rangle(z) = \frac{\epsilon_{\text{CII}}}{4\pi\nu_{\text{rest,CII}}} \frac{c}{H(z)}, \quad (22)$$

where ϵ_{CII} denotes the average co-moving emissivity (luminosity density) in the line, and $\nu_{\text{rest,CII}}$ is the rest frame frequency of the [CII] line. We have further assumed a delta function [CII] line emission profile.

The one-to-one relation between [CII] luminosity and star-formation rate (SFR) we adopt is:

$$L = L_0 \frac{\text{SFR}}{1 M_\odot \text{yr}^{-1}}, \quad (23)$$

with $L_0 = 6 \times 10^6 L_\odot$ (Righi et al. 2008; Visbal & Loeb 2010). We neglect any redshift evolution in L_0 (see e.g. Lidz & Taylor 2016 for a discussion). We assume that the abundance of galaxies as a function of their SFR obeys a Schechter function form (Schechter 1976):

$$\phi(\text{SFR}) d\text{SFR} = \phi_* \left(\frac{\text{SFR}}{\text{SFR}_*} \right)^\alpha \exp \left[-\frac{\text{SFR}}{\text{SFR}_*} \right] \frac{d\text{SFR}}{\text{SFR}_*}. \quad (24)$$

Here α denotes the faint-end slope, while ϕ_* and SFR_* are characteristic number densities and SFRs. The co-moving [CII] emissivity is then:

$$\epsilon_{\text{CII}} = \phi_* L_0 \frac{\text{SFR}_*}{1 M_\odot \text{yr}^{-1}} \Gamma(2 + \alpha). \quad (25)$$

We use the Schechter SFR function parameters in Smit et al. (2012), determined using dust-corrected ultraviolet luminosity functions at redshifts of $z = 2.2, 3.8, 5.0, 5.9, 6.8$. We find that the following functional form provides a reasonable approximation to the redshift evolution of the Schechter parameters:

$$\begin{aligned} \alpha &= -1.96 \\ \text{SFR}_*(z) &= 134.39 z^{-1.18} M_\odot \text{yr}^{-1} \\ \phi_*(z) &= 0.00358 z^{-0.85} \text{Mpc}^{-3}. \end{aligned} \quad (26)$$

This procedure allows us to compute $\langle I_{\text{CII}} \rangle$ at each relevant redshift. We find: $\langle I_{\text{CII}} \rangle = 3.1 \times 10^2 \text{ Jy/str}, 7.1 \times 10^2 \text{ Jy/str}, 1.1 \times 10^3 \text{ Jy/str}$ for $z = 9.41, 7.37, 6.43$, respectively.

6.2. SNR Formula

In order to estimate the signal-to-noise ratio (SNR), we require a formula for the cross-bispectrum variance, $\text{Var}[Q_{21,\text{CII},\text{CII}}]$. In calculating the variance, we suppose that the [CII] and 21 cm fluctuation fields obey Gaussian statistics. The variance of the cross-bispectrum (for $k_1 \neq k_2 \neq k_3$) is (see e.g. Greig et al. 2013; Joachimi et al. 2009 for related calculations):

$$\begin{aligned} \text{Var}[B_{21,\text{CII},\text{CII}} + 2 \text{ perm.}] &= \\ \frac{V_s}{N_t} (P_{\text{tot},21}(k_1) P_{\text{tot},\text{CII}}(k_2) P_{\text{tot},\text{CII}}(k_3) + 2 \text{ perm.}), \end{aligned} \quad (27)$$

where $P_{\text{tot}} = P + N$ is the total signal plus detector noise auto-power spectrum for each of the 21 cm and [CII] emission fields. The noise power spectrum for the 21 cm survey is subsequently denoted by N_{21} and the [CII] noise power by N_{CII} . We neglect contributions to the variance from residual foregrounds. Later we will add in the permutations on k_1, k_2 , and k_3 . Note that if any of k_1, k_2 , or k_3 are equal, there are extra terms (which we write down explicitly in Appendix B). These extra terms are what give rise to the symmetry factor, s_B , in Greig et al. (2013) and related works.

Now, we use propagation of errors to recover $\text{Var}[Q]$,

$$\begin{aligned} \text{Var}[Q] &= \left(\frac{\partial Q}{\partial B} \right)^2 \text{Var}[B] \\ &+ \sum_{i=1}^3 \left(\frac{\partial Q}{\partial P(k_i)} \right)^2 \text{Var}[P(k_i)] \\ &+ \sum_{j=1}^3 \frac{\partial Q}{\partial P(k_j)} \frac{\partial Q}{\partial B} \text{Cov}[B, P(k_j)], \end{aligned} \quad (28)$$

where the summations i and j span the three wavevector arguments, k_1, k_2 , and k_3 . Under the Gaussian approximation adopted here, $\text{Cov}[B, P(k_i)]$ vanishes because it is a five-point function with vanishing unconnected pieces. Furthermore, we suppose that the term involving

$\text{Var}[P(k_i)]$ is sub-dominant and neglect it in what follows. Finally, accounting for wavevector permutations, we arrive at our formula for the variance on Q :

$$\text{Var}[Q] = \frac{V_s}{N_t} \frac{(P_{\text{tot},21}(k_1)P_{\text{tot,CII}}(k_2)P_{\text{tot,CII}}(k_3) + 2 \text{ perm.})}{9(P_{21,\text{CII}}(k_1)P_{21,\text{CII}}(k_2) + 2 \text{ perm.})^2}, \quad (29)$$

where V_s is the survey volume, and N_t is the number of triangles, which we will derive shortly. Note that the $1/9$ factor comes from the $1/3$ in our definition of $Q_{21,\text{CII},\text{CII}}$ in Eq. 13

In order to estimate the expected error bars on the parameters of interest, specifically $\langle T_{21} \rangle b_{21}$ and $C_{21,\text{CII},\text{CII}}$, we use the Fisher matrix formalism. The Fisher matrix is calculated as (e.g. Greig et al. 2013):

$$F_{ij} = \sum_{k_1 \leq k_2 \leq k_3} \frac{1}{\text{Var}[Q](A, N_{21}, N_{\text{CII}})} \frac{\partial Q}{\partial \theta_i} \frac{\partial Q}{\partial \theta_j}, \quad (30)$$

where θ_i denotes our two model parameters ($\langle T_{21} \rangle b_{21}$ and $C_{21,\text{CII},\text{CII}}$).

6.3. Survey Parameters

We adopt a simple, yet flexible, description for the upcoming 21 cm and [CII] surveys. First, we assume that the noise power spectrum for each survey is well-approximated by isotropic, white-noise. In detail, this is an imperfect approximation, especially for the interferometric 21 cm observations in which case the noise power is a strong function of k_\perp ; in reality, the 21 cm noise power is sensitive to the precise distribution of interferometric baselines. Our estimates here should be refined in future work. In our fiducial model, we match the amplitude of the white-noise power spectrum in each of the 21 cm and [CII] fields to their signal power at $k = 0.05 \text{ Mpc}^{-1}$, i.e. we set $N_{21} = P_{21,21}$ at this wavenumber, and similarly for N_{CII} . This amounts to assuming that larger spatial scales are sample-variance dominated, while smaller-scales are limited by detector noise. For the survey volume, we assume that a common survey area, A_{survey} , is shared between the 21 cm and [CII] surveys, and adopt a redshift bin width of $\Delta z = 0.3$. Our fiducial model takes $A_{\text{survey}} = 50 \text{ deg}^2$.

The number of triangles (with wavevectors within a given range) that fit into the overlap region of the two surveys may be calculated as:

$$N_t = \frac{V_B}{V_{\text{fund}}^2}. \quad (31)$$

Here V_B is the 6D Fourier volume satisfying $\mathbf{k}_1 + \mathbf{k}_2 + \mathbf{k}_3 = \mathbf{0}$ of the 9D Fourier space spanned by $(\mathbf{k}_1, \mathbf{k}_2, \mathbf{k}_3)$. More specifically,

$$V_B \equiv \int_{k_1} d^3 q_1 \int_{k_2} d^3 q_2 \int_{k_3} d^3 q_3 \delta_D(\mathbf{q}_1 + \mathbf{q}_2 + \mathbf{q}_3), \quad (32)$$

where \int_{k_i} refers to the integral over a wavevector bin centered around $|\mathbf{q}_i| = |\mathbf{k}_i|$. Assuming that $k_1 \geq k_2 \geq k_3$, one can show that (e.g. Greig et al. (2013)),

$$V_B \simeq 8\pi^2 k_1 k_2 k_3 (\Delta k)^3 \theta(k_1, k_2, k_3), \quad (33)$$

where,

$$\theta(k_1, k_2, k_3) = \begin{cases} \frac{1}{2} & \text{if } k_i = k_j + k_k \\ 1 & \text{if } k_i \neq k_j + k_k, \end{cases} \quad (34)$$

is a symmetry factor ensuring that equivalent modes are not double counted. We adopt a bin size of $\Delta k = 0.03 \text{ Mpc}^{-1}$. The quantity V_{fund} in Eq. 31 denotes the k -space volume spanned by the fundamental modes of the joint survey regions. For this, we assume that the joint survey area is a square, giving:

$$V_{\text{fund}} = \frac{(2\pi)^3}{L_\perp^2 L_\parallel} \quad (35)$$

where L_\perp and L_\parallel are the co-moving extent of the survey volume perpendicular, parallel to the line of sight. We calculate L_\perp at the central redshift of each redshift bin.

We then proceed to calculate the expected SNR on $\langle T_{21} \rangle b_{21}$, marginalizing over $C_{21,21,21}$, using the inverse Fisher matrix (Eq. 30). We perform these calculations at each of three different redshifts, while varying the survey parameters, N_{CII} , A_{survey} , and N_{21} around our fiducial values to explore how our forecasts depend on these inputs.

The results of these calculations are shown in Fig. 8. These estimates are generally encouraging: for example, in order to achieve a $10 - \sigma$ detection (i.e. $\text{SNR} = 10$) of the 21 cm-[CII]-[CII] bispectrum near the mid-point of reionization (at $z = 7.37$ in this model) a 50 deg^2 survey with $N_{\text{CII}} \lesssim 1.6 \times 10^8 (\text{Jy/sr})^2 \text{ Mpc}^3$ is required. This is more demanding than the noise expected for the ‘‘Stage II’’ [CII] survey described in Silva et al. (2015) which has a noise power spectrum of $N_{\text{CII}} \sim 2.5 \times 10^9 (\text{Jy/sr})^2 \text{ Mpc}^3$ at $z = 7$ (Lidz & Taylor 2016). Nonetheless, this improved sensitivity may be achievable with future improvements in detector technology, for example. As quantified in the figure, the requirements are somewhat less stringent at $z = 6.43$ and somewhat more so at $z = 9.41$. Note that our model assumes that the $L_{\text{CII-SFR}}$ relation is independent of redshift. This assumption is most suspect for this highest redshift bin, since the galaxies at this early time may have low metallicities and little [CII] emission. In any case, none of the currently planned [CII] emission surveys target such high redshifts (Kovetz et al. 2017). The requirements on the 21 cm thermal noise appear less severe, with the $\text{SNR}(\langle T_{21} \rangle b_{21})$ saturating for $N_{21} \lesssim 10^5 \text{ mK}^2 \text{ Mpc}^3$. The results are less sensitive to the 21 cm noise power spectrum than the [CII] noise both because our cross-bispectrum involves only one 21 cm field (yet two [CII] fields) and since the 21 cm power spectrum becomes sample-variance limited at the wavenumbers of interest. The latter fact explains the saturation in the SNR with decreasing N_{21} . The required N_{21} seems feasible since HERA-350 will image some large-scale modes (DeBoer et al. 2017), implying that sample-variance limited sensitivity will be achieved on large scales.

Another approach for improving the $\text{SNR}(\langle T_{21} \rangle b_{21})$ is to increase the joint sky-coverage. For example, one possibility is to measure the 21 cm-Ly- α -Ly- α bispectrum (rather than the 21 cm-[CII]-[CII] bispectrum considered here). This may be feasible with the planned all-sky survey SPHEREX (Doré et al. 2018), in which case one

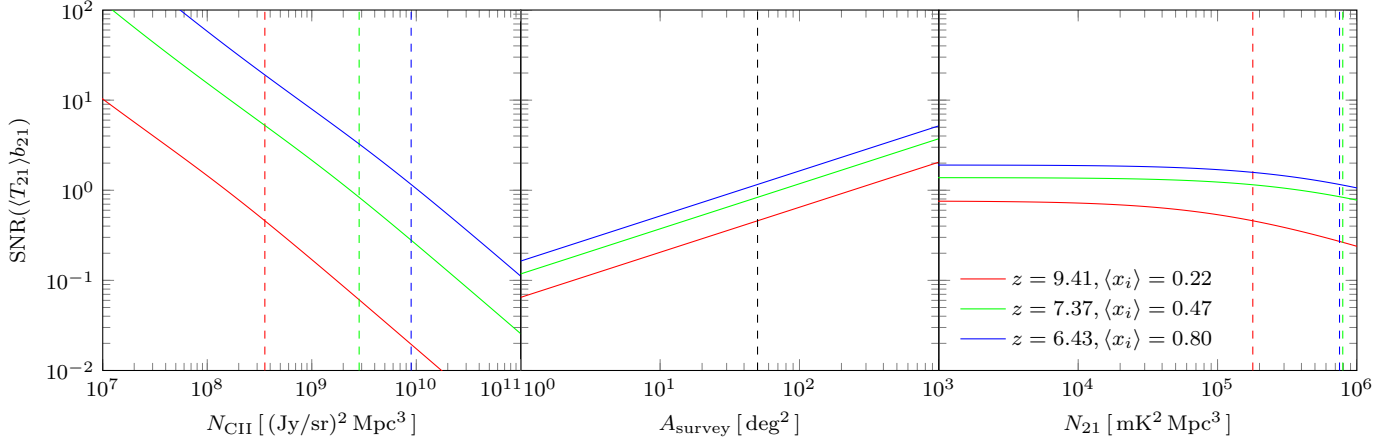


FIG. 8.— Estimated SNR of $Q_{21,\text{CII},\text{CII}}$ as a function of (*Left-hand panel*) N_{CII} , (*Middle panel*) A_{survey} , and (*Right-hand panel*) N_{21} . When not varied, we assumed that $N_{\text{CII}} = P_{\text{CII},\text{CII}}$ at $k = 0.05 \text{ Mpc}^{-1}$, $A_{\text{survey}} = 50 \text{ deg}^2$ and $N_{21} = P_{21,21}$ at $k = 0.05 \text{ Mpc}^{-1}$. Fiducial values are given by vertical dashed lines in each plot – for N_{21} and N_{CII} these are redshift dependent.

could match the entire $\sim 1440 \text{ deg}^2$ coverage of HERA-350 (DeBoer et al. 2017). The figure illustrates that our forecasts improve dramatically for wider survey areas.

To further explore the potential reach of our method, we consider more futuristic surveys and plot $1 - \sigma$ contours in the $\langle T_{21} \rangle b_{21} - C_{21,\text{CII},\text{CII}}$ plane at different redshifts in Fig. 9. In this case, we set the joint survey area to be $A = 1000 \text{ deg}^2$ and we match N_{21} and N_{CII} to P_{21} and P_{CII} at $k = 0.1 \text{ Mpc}^{-1}$. This corresponds to noise values of $N_{21} = 1.7 \times 10^5, 2.6 \times 10^5, 7.6 \times 10^5 \text{ mK}^2 \text{ Mpc}^3$, and $N_{\text{CII}} = 3.4 \times 10^9, 1.1 \times 10^9, 1.4 \times 10^8 \text{ (Jy/sr)}^2 \text{ Mpc}^3$ at $z = 6.43, 7.37, 9.41$. This survey should indeed enable a sharp test of the “rise and fall” behavior from the cross-bispectrum. The contours also help illustrate the level of degeneracy between $\langle T_{21} \rangle b_{21}$ and $C_{21,\text{CII},\text{CII}}$; these parameters are less covariant during the middle of reionization (when $\langle T_{21} \rangle b_{21}$ is large). This results because $Q_{21,\text{CII},\text{CII}}$ has a flatter dependence on θ_{12} at this stage of reionization, which makes it easier to estimate $C_{21,\text{CII},\text{CII}}$.

7. CONCLUSIONS

Our aim in this work has been to help circumvent two of the primary challenges associated with 21 cm fluctuation measurements of the EoR. The two concerns are that: residual foregrounds may produce errors in the inferred 21 cm auto-spectrum (or lead to a spurious detection), and that the 21 cm auto-spectrum is itself difficult to interpret given our imperfect models of the EoR. The first issue may, in part, be side-stepped by cross-correlating 21 cm fluctuation measurements with an additional tracer of the high redshift universe, such as line-intensity mapping data cubes in the [CII] emission line. The second concern is, in part, alleviated by identifying statistics that are amenable to an analytic treatment.

Here, we proposed that the 21 cm-[CII]-[CII] cross-bispectrum may help in both regards. First, residual foregrounds only impact the variance of the cross-bispectrum and not the ensemble average (modulo foregrounds that are common to the two surveys.) Second, we showed that the configuration dependence of the 21 cm- $\delta\delta$ cross-bispectrum (a proxy for the 21 cm-[CII]-[CII] cross-bispectrum which is more challenging to simulate) is fairly well described by second-order perturbation

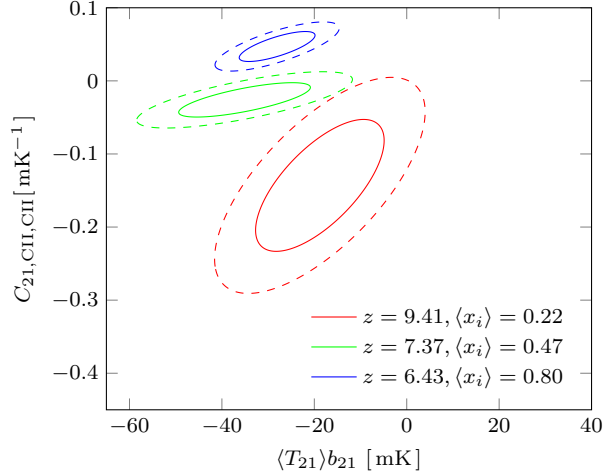


FIG. 9.— Forecasted constraints in the $\langle T_{21} \rangle b_{21} - C_{21,\text{CII},\text{CII}}$ plane at different redshifts. The solid/dashed ellipses show the expected $1 - \sigma/2 - \sigma$ contours at different redshifts, with each contour centered on the values of $\langle T_{21} \rangle b_{21}$ and $C_{21,\text{CII},\text{CII}}$ in our simulated models. These forecasts assume an ambitious, futuristic survey, with a sky coverage of $A = 1000 \text{ deg}^2$ and low detector noise with N_{21} and N_{CII} matching P_{21} and P_{CII} at the scale of $k = 0.1 \text{ Mpc}^{-1}$ (see text).

theory, especially provided one considers large spatial scales before the ionization fraction reaches $\langle x_i \rangle \sim 0.7$. Further, this may be used to extract the redshift evolution of $\langle T_{21} \rangle b_{21}$ without resorting to reionization simulations. While such simulations are nevertheless required to understand the full implications of the $\langle T_{21} \rangle b_{21}$ measurements for the reionization history and the properties of the ionizing sources, we believe it is still valuable to consider upcoming 21 cm measurements in the context of cosmological perturbation theory. For example, the redshift evolution of $\langle T_{21} \rangle b_{21}$ inferred (on large scales) from the 21 cm auto-power spectrum, the 21 cm auto-bispectrum, and the 21 cm-[CII]-[CII] cross-bispectrum should each show the “rise and fall” signature. More generally, demonstrating the consistency of inferences from two and three-point statistics should help in establishing the robustness of initial 21 cm detections. Unsurprisingly, the perturbative description is imperfect and future simulation efforts may help in exploiting informa-

tion on small spatial scales, especially during the late stages of reionization.

We made rough estimates of the survey specifications required to detect the 21 cm-[CII]-[CII] cross-bispectrum. Assuming a joint survey area of $A_{\text{survey}} = 50 \text{ deg}^2$, we found that a detection generally requires a more sensitive [CII] survey than the Stage-II [CII] emission survey described in Silva et al. (2015). It would be interesting to refine our analysis by considering a more detailed treatment of the noise in each survey, by quantifying the impact of residual foregrounds on the cross-bispectrum variance, and by exploring to what extent foregrounds may be shared by the two surveys. Since the perturbative description is accurate on large spatial scales, this approach is most valuable if measurements can be made robustly at small wavenumbers ($k \lesssim 0.05 - 0.1 \text{ Mpc}^{-1}$).

In terms of modeling, we showed that the L-PICOLA code may be used in conjunction with 21cmFAST (replacing the Zel'dovich generated density field used in 21cmFAST by default) to improve the treatment of three-point statistics in EoR calculations, at only modest additional computational expense. In the future, it would be interesting to include a more detailed model for the [CII]-emission fluctuations: it is challenging to capture

the large spatial scales of interest for our bispectrum calculations, while simultaneously resolving the small mass halos hosting [CII]-emitting galaxies. We considered only a single representative reionization model: we expect the perturbative description to work better if the ionized regions are smaller than in this model, while it will perform less well in scenarios with larger bubbles. While we considered only the 21 cm and [CII] emission lines in this work, the same methodology may be applied to other emission lines and it will be interesting to consider these prospects. In summary, higher-order statistics should help in extracting key information about the EoR from upcoming surveys.

ACKNOWLEDGEMENTS

We thank the anonymous referee for providing helpful comments. We would like to thank Matthew McQuinn for helpful comments on a draft of this paper. AB would like to thank Congzhou M. Sha for helpful comments on code used in this work, and Todd Phillips for helpful discussions. AB was supported by the Roy & Diana Vagelos Program in the Molecular Life Sciences and the Roy & Diana Vagelos Challenge Award.

REFERENCES

- Becker, G. D., Bolton, J. S., & Lidz, A. 2015, *PASA*, 32, e045
 Becker, R. H., Fan, X., White, R. L., et al. 2001, *AJ*, 122, 2850
 Bernardeau, F., Colombi, S., Gaztanaga, E., & Scoccimarro, R. 2002, *Phys. Rept.*, 367, 1
 Bharadwaj, S., & Pandey, S. K. 2005, *Mon. Not. Roy. Astron. Soc.*, 358, 968
 Bond, J. R., Cole, S., Efstathiou, G., & Kaiser, N. 1991, *Astrophys. J.*, 379, 440
 Chung, D. T., Li, T. Y., Viero, M. P., Church, S. E., & Wechsler, R. H. 2017, *Astrophys. J.*, 846, 60
 Crites, A. T., Bock, J. J., Bradford, C. M., et al. 2014, in *Proc. SPIE*, Vol. 9153, Millimeter, Submillimeter, and Far-Infrared Detectors and Instrumentation for Astronomy VII, 91531W
 Crocce, M., Pueblas, S., & Scoccimarro, R. 2006, *MNRAS*, 373, 369
 DeBoer, D. R., Parsons, A. R., Aguirre, J. E., et al. 2017, *PASP*, 129, 045001
 Dekel, A., & Lahav, O. 1999, *Astrophys. J.*, 520, 24
 Dillon, J. S., et al. 2014, *Phys. Rev.*, D89, 023002
 Doré, O., Werner, M. W., Ashby, M., et al. 2016, *ArXiv e-prints*, arXiv:1606.07039
 Doré, O., Werner, M. W., Ashby, M. L. N., et al. 2018, *ArXiv e-prints*, arXiv:1805.05489
 Fan, X., Strauss, M. A., Richards, G. T., et al. 2006, *AJ*, 131, 1203
 Fry, J. N. 1994, *Phys. Rev. Lett.*, 73, 215
 Furlanetto, S., & Lidz, A. 2007, *Astrophys. J.*, 660, 1030
 Furlanetto, S., Zaldarriaga, M., & Hernquist, L. 2004, *Astrophys. J.*, 613, 1
 Furlanetto, S. R., Zaldarriaga, M., & Hernquist, L. 2004, *ApJ*, 613, 1
 Gong, Y., Cooray, A., Silva, M., et al. 2012, *ApJ*, 745, 49
 Gong, Y., Cooray, A., Silva, M. B., Santos, M. G., & Lubin, P. 2011, *ApJ*, 728, L46
 Greig, B., Komatsu, E., & Wyithe, J. S. B. 2013, *MNRAS*, 431, 1777
 Hoffmann, K., Mao, Y., Mo, H., & Wandelt, B. D. 2018, *ArXiv e-prints*, arXiv:1802.02578
 Howlett, C., Manera, M., & Percival, W. J. 2015, *Astronomy and Computing*, 12, 109
 Jensen, H., et al. 2013, *Mon. Not. Roy. Astron. Soc.*, 435, 460
 Joachimi, B., Shi, X., & Schneider, P. 2009, *A&A*, 508, 1193
 Kovetz, E. D., Viero, M. P., Lidz, A., et al. 2017, *ArXiv e-prints*, arXiv:1709.09066
 Lagache, G. 2017, *IAU Symp.*, 333, 228
 Leclercq, F., Jasche, J., Gil-Marín, H., & Wandelt, B. 2013, *J. Cosmology Astropart. Phys.*, 11, 048
 Lidz, A., Furlanetto, S. R., Oh, S. P., et al. 2011, *ApJ*, 741, 70
 Lidz, A., & Taylor, J. 2016, *ApJ*, 825, 143
 Lidz, A., Zahn, O., Furlanetto, S., et al. 2009, *Astrophys. J.*, 690, 252
 Lidz, A., Zahn, O., McQuinn, M., Zaldarriaga, M., & Hernquist, L. 2008, *ApJ*, 680, 962
 Loeb, A., & Furlanetto, S. R. 2013, *The First Galaxies in the Universe* (Princeton University Press)
 Majumdar, S., Pritchard, J. R., Mondal, R., et al. 2018, *MNRAS*, 476, 4007
 Matarrese, S., Verde, L., & Heavens, A. F. 1997, *Mon. Not. Roy. Astron. Soc.*, 290, 651
 McQuinn, M., Lidz, A., Zahn, O., et al. 2007, *MNRAS*, 377, 1043
 Mesinger, A., & Furlanetto, S. 2007, *Astrophys. J.*, 669, 663
 Mesinger, A., Furlanetto, S., & Cen, R. 2011, *MNRAS*, 411, 955
 Planck Collaboration, Ade, P. A. R., Aghanim, N., et al. 2016a, *A&A*, 594, A13
 Planck Collaboration, Adam, R., Aghanim, N., et al. 2016b, *A&A*, 596, A108
 Pritchard, J. R., & Furlanetto, S. R. 2007, *Mon. Not. Roy. Astron. Soc.*, 376, 1680
 Pullen, A. R., Dore, O., & Bock, J. 2014, *Astrophys. J.*, 786, 111
 Righi, M., Hernández-Monteagudo, C., & Sunyaev, R. A. 2008, *A&A*, 489, 489
 Schechter, P. 1976, *ApJ*, 203, 297
 Scherrer, R. J., & Weinberg, D. H. 1998, *Astrophys. J.*, 504, 607
 Scoccimarro, R. 1997, *ApJ*, 487, 1
 Scoccimarro, R., Feldman, H. A., Fry, J. N., & Frieman, J. A. 2001, *Astrophys. J.*, 546, 652
 Shimabukuro, H., Yoshiura, S., Takahashi, K., Yokoyama, S., & Ichiki, K. 2016, *Mon. Not. Roy. Astron. Soc.*, 458, 3003
 —. 2017, *Mon. Not. Roy. Astron. Soc.*, 468, 1542
 Silva, M., Santos, M. G., Cooray, A., & Gong, Y. 2015, *ApJ*, 806, 209
 Smit, R., Bouwens, R. J., Franx, M., et al. 2012, *ApJ*, 756, 14
 Smith, R. E., Sheth, R. K., & Scoccimarro, R. 2008, *Phys. Rev.*, D78, 023523
 Springel, V. 2005, *Mon. Not. Roy. Astron. Soc.*, 364, 1105
 Tassev, S., Zaldarriaga, M., & Eisenstein, D. J. 2013, *J. Cosmology Astropart. Phys.*, 6, 036
 Venemans, B. P., Findlay, J. R., Sutherland, W. J., et al. 2013, *ApJ*, 779, 24

Verde, L., et al. 2002, Mon. Not. Roy. Astron. Soc., 335, 432
Visbal, E., & Loeb, A. 2010, J. Cosmology Astropart. Phys., 11,
016

Zahn, O., Lidz, A., McQuinn, M., et al. 2006, Astrophys. J., 654,
12
Zaldarriaga, M., Furlanetto, S. R., & Hernquist, L. 2004,
Astrophys. J., 608, 622
Zel'dovich, Y. B. 1970, A&A, 5, 84

APPENDIX A: 21CM BIAS RESULTS

Here we show how our $\langle T_{21} \rangle b_{21}$ results vary for different choices of k_{\min} and k_{\max} (Fig. 10). As discussed in § 3.4, the results are noisy for small k_{\min} , while the perturbative description breaks down when k_{\max} is too large.

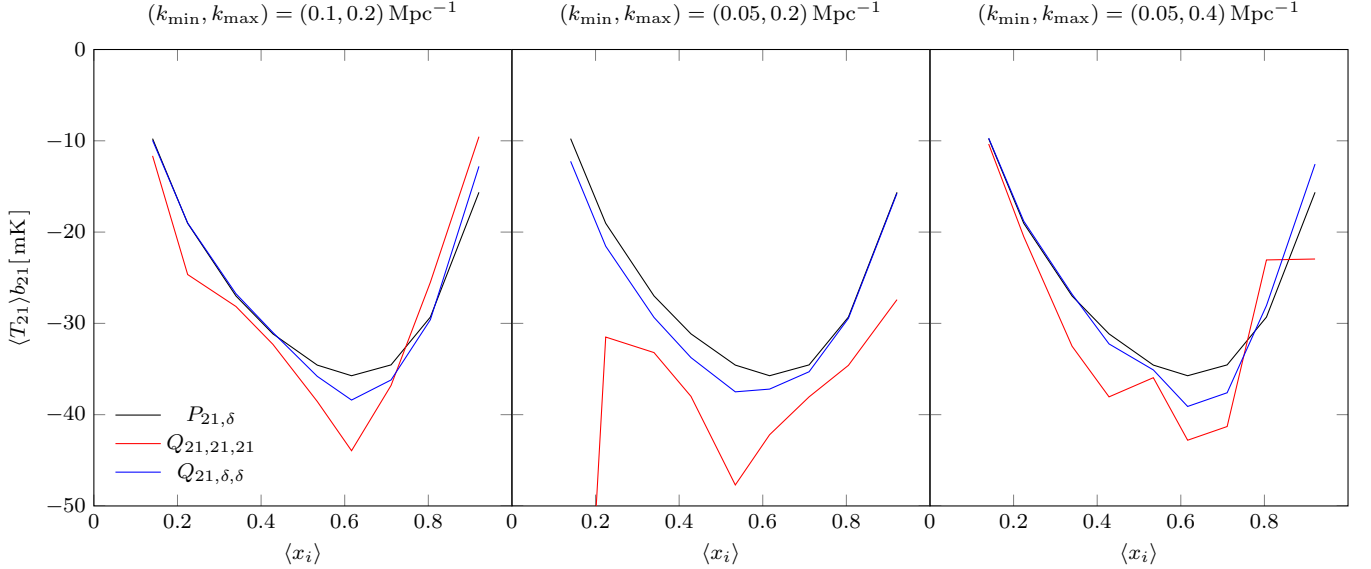


FIG. 10.— Consistency between different estimates of $\langle T_{21} \rangle b_{21}$. The black curves show the linear 21 cm bias factor, $\langle T_{21} \rangle b_{21}$, inferred from the cross-power spectrum, $\langle T_{21} \rangle b_{21} = P_{21,\delta}/P_{\delta,\delta}$ on large scales, as a function of $\langle x_i \rangle$. These are compared with the linear bias inferred from $Q_{21,21,21}$ (red) and $Q_{21,\delta,\delta}$ (blue). *Left, Center:* Extracted $\langle T_{21} \rangle b_{21}$ for two different values of k_{\min} and k_{\max} . *Right:* The plot from Fig. 5 is reproduced here for convenience. Note that the values of $\langle T_{21} \rangle b_{21}$ inferred from the 21 cm auto-bispectrum at low $\langle x_i \rangle$ show a marked difference from the cross-power spectrum and cross-bispectrum inferences in the *Central panel*. We believe this relates to the early-phase transition in the sign of the 21 cm-density cross-correlation coefficient (see § 3.2)

APPENDIX B: CROSS-BISPECTRUM VARIANCE

Here we write down a formula for the cross-bispectrum variance in the case that some of the k -modes have equal magnitude. See e.g. Joachimi et al. (2009) for more details. Recall that we have enforced $k_1 \geq k_2 \geq k_3$.

$$\text{Var}[B_{21,\text{CII},\text{CII}} + 2 \text{ perm.}] = \begin{cases} P_{\text{tot},21}(k_1)P_{\text{tot},\text{CII}}(k_2)P_{\text{tot},\text{CII}}(k_3) + 2 \text{ perm.} & \text{if } k_1 \neq k_2 \neq k_3 \\ \begin{aligned} &2P_{\text{tot},21}(k_3)P_{\text{tot},\text{CII}}(k_1)^2 \\ &+ 2P_{\text{tot},21}(k_1)P_{\text{tot},\text{CII}}(k_3)P_{\text{tot},21}(k_1) \\ &+ 2P_{21,\text{CII}}(k_1)^2P_{\text{tot},\text{CII}}(k_3) \end{aligned} & \text{if } k_1 = k_2 \neq k_3 \\ \begin{aligned} &2P_{\text{tot},21}(k_1)P_{\text{tot},\text{CII}}(k_2)^2 \\ &+ 2P_{\text{tot},21}(k_2)P_{\text{tot},\text{CII}}(k_1)P_{\text{tot},21}(k_2) \\ &+ 2P_{21,\text{CII}}(k_2)^2P_{\text{tot},\text{CII}}(k_1) \end{aligned} & \text{if } k_1 \neq k_2 = k_3 \\ \begin{aligned} &6P_{\text{tot},21}(k_1)P_{\text{tot},\text{CII}}(k_1)P_{\text{tot},\text{CII}}(k_1) \\ &+ 12P_{21,\text{CII}}(k_1)^2P_{\text{tot},\text{CII}}(k_1) \end{aligned} & \text{if } k_1 = k_2 = k_3 \end{cases} \quad (36)$$